FISEVIER

Contents lists available at ScienceDirect

### Journal of Alloys and Compounds

journal homepage: www.elsevier.com/locate/jalcom



# Enhanced solar-driven hydrogen evolution over ultrathin g-C<sub>3</sub>N<sub>4</sub>/ReSe<sub>2</sub> heterojunction-like nanosheets with surface selenium vacancies



Zhengyun Wang<sup>a</sup>, Fengyi Yang<sup>a</sup>, Tao Ding<sup>b</sup>, Ming-Hsien Lee<sup>c</sup>, Qing Yang<sup>a,\*</sup>

- <sup>a</sup> Hefei National Research Center of Physical Sciences at the Microscale & Department of Chemistry, University of Science and Technology of China (USTC), Hefei 230026, Anhui, PR China
- <sup>b</sup> National Synchrotron Radiation Laboratory, USTC, Hefei 230026, Anhui, PR China
- <sup>c</sup> Department of Physics, Tamkang University, New Taipei City 251301, Taiwan, Republic of China

#### ARTICLE INFO

Article history:
Received 14 March 2022
Received in revised form 30 May 2022
Accepted 4 June 2022
Available online 7 June 2022

Keywords:
Graphitic carbon nitride
Rhenium selenide
Photocatalysis
Selenium-vacancy
Electronic structural modulation
Two-dimensionalization

#### ABSTRACT

The design of composite photocatalytic materials is essential for efficient photocatalytic hydrogen production. In the present work, we have successfully designed a simple synthetic process to ultrathin ReSe<sub>2</sub> nanosheets using an ultrasound-assisted liquid-phase synthetic route through self-assembling ReSe<sub>2</sub> onto g-C<sub>3</sub>N<sub>4</sub> (shortened as g-C<sub>3</sub>N<sub>4</sub>/ReSe<sub>2</sub> nanosheets) to improve photocatalytic performance. Based on density functional theory (DFT) estimation along with experimental characterization, it is found that the integrated heterojunction-like ultrathin g-C<sub>3</sub>N<sub>4</sub>/ReSe<sub>2</sub> nanosheets possess more edge active sites, enhanced electron transfer efficiency and conductivities, which significantly accelerates the dissociation and migration of photogenerated electron-hole pairs. Meanwhile, selenium vacancies could be introduced into nanosheets via controlling the synthetic procedure with a reduced Se source that will favor to enhance the photocatalytic efficiency. The ultrathin g-C<sub>3</sub>N<sub>4</sub>/ReSe<sub>2</sub> heterojunction with Se vacancies performed highly improved photocatalytic hydrogen production. In typical, the H<sub>2</sub> production of the g-C<sub>3</sub>N<sub>4</sub>/ReSe<sub>2</sub> nanosheets under visible light is  $1055.50 \,\mu$ mol g<sup>-1</sup> h<sup>-1</sup>, which is 21 times higher than that of bare g-C<sub>3</sub>N<sub>4</sub>, indicating that it overcomes the high charge complexation rate of g-C<sub>3</sub>N<sub>4</sub>. These results do not only provide insight into the application of two-dimensional ReSe<sub>2</sub> nanosheets in photocatalysis, but also open up new avenues for the rational design of two-dimensional hybrid materials in solar energy conversion.

© 2022 Published by Elsevier B.V.

#### 1. Introduction

Compared with traditional fossil energy, hydrogen energy is promising due to its pollution-free and high energy density [1–5]. At present, most hydrogen production is still reproduced from fossil fuels, which greatly limits the exploitation and application of hydrogen energy. Hence, it is foreseeable that renewable techniques of hydrogen energy production especially from water decomposition will be one of the ultimate solutions [6–8].

Photocatalytic water splitting based on various semiconducting photocatalysts with suitable bandgaps is one of the most viable methods to generate hydrogen that has been exploited for practical applications [9–13]. Due to its suitable energy band structure, simple preparation process, strong visible light absorption ability, and good physicochemical stability, nonmetallic semiconducting  $g-C_3N_4$  is one of the most promising photocatalysts for hydrogen evolution

limited visible light absorption, and low specific surface area [3,5,10,16]. To develop an efficient g-C<sub>3</sub>N<sub>4</sub>-based nanocomposite, there should be some special properties like narrow energy bands, capable of absorbing visible light in the solar spectra, and energy band positions suitable for efficient redox reactions required. In general, it is difficult to meet the requirements for hydrogen production efficiently by using a singular type of semiconductors. As noted, heterostructured photocatalysts composited of different components could cover an enwidened range of light absorption with the corresponding integrated composition, bandgap overlaps/ modulations, and enhanced charge separation at the junction interface [3,5,10,16]. Meanwhile, the band alignment including band bending of the composites with heterojunction-like structure drives the separation and reverse charge transfer of photogenerated electrons and holes, inhibiting charge recombination and improving the catalytic activity [8,17-19].

[14–16]. However, it is still limited in commercialization as a high-efficiency photocatalyst, due to its rapid carrier recombination,

<sup>\*</sup> Corresponding author.

E-mail address: qyoung@ustc.edu.cn (Q. Yang).

Transition metal dichalcogenides (TMDs) are a class of semiconductors with graphene-like layered structure and adjustable bandgaps. In particular, bulk MoS2 is an indirect bandgap semiconductor with a bandgap width of 1.3 eV. However, as the number of layers decreases, the single-layer MoS<sub>2</sub> nanosheet transitions from indirect bandgap structure to direct bandgap one with a bandgap of 1.8 eV [20]. Moreover, due to the quantum confinement and surface effect, monolayer TMDs exhibit different properties from bulk materials. For example, monolayer MoS<sub>2</sub> has the ability to reduce H<sup>+</sup> to H<sub>2</sub>, which makes ultrathin TMDs have broad prospective applications in the field of photocatalysis [21,22]. On the other hand, due to the elasticity of two-dimensional morphology, g-C<sub>3</sub>N<sub>4</sub> can perfectly form heterojunction-like photocatalysts interfaces with various 2D TMDs components. Therefore, it is vital to construct new heterojunction-like materials through the combination of TMDs and g- $C_3N_4$  [23,24].

As an emerging portion of TMDs, ReSe<sub>2</sub>, different from the common hexagonal TMDs, presents a distorted 1 T' form and has unique electrical/optical properties [25,26]. In recent years, ReSe<sub>2</sub> has attracted extensive attention in the fields of catalysis, electronics, and optoelectronics. Theoretical calculations and experiments show that its microstructure and electronic structure can be adjusted and electrocatalytic activity improved through vacancy engineering [27,28]. However, there is not sufficient study on ReSe<sub>2</sub> via establishing heterostructured catalysts for photocatalytic hydrogen evolution for possible reference.

Herein, we developed a simple and rapid procedure to synthesize ultrathin  $\operatorname{ReSe}_2$  nanosheets with rich atomic level edge active sites, and further form heterostructured nanosheets of  $\operatorname{ReSe}_2$  with  $\operatorname{g-C}_3N_4$  as a heterojunction-type photocatalyst. Based on density functional theory (DFT), the physicochemical properties of the nanosheets were studied at the atomic level simultaneously [29–34]. Furthermore, according to the previous research in the electrochemical catalysis of our research group, suitable selenium vacancies were introduced to further improve the photocatalytic performance of heterojunction [28]. As revealed in the present study, the preparation of  $\operatorname{ReSe}_2$  ultrathin nanosheets by combining defect engineering has proved to be an effective and feasible way to improve the photocatalytic properties of the active materials of  $\operatorname{g-C}_3N_4$ .

#### 2. Experimental section

#### 2.1. Materials synthesis

#### 2.1.1. Fabrication of $g-C_3N_4$ nanoparticles

g-C<sub>3</sub>N<sub>4</sub> was prepared by pyrolysis of carbamide in a muffle furnace at 550 °C for 3 h (heating rate of 5 °C min<sup>-1</sup>). Then, collected the light-yellow powder and annealed at 350 °C gradually in Ar (heating rate of 5 °C min<sup>-1</sup>). The annealed g-C<sub>3</sub>N<sub>4</sub> sample was washed several times in distilled water with ultrasonic cleaning equipment.

2.1.2. Fabrication of  $ReSe_2$  and selenium vacancy-containing  $ReSe_2$  ( $ReSe_2$ (SV)) ultrathin nanosheets

The bulk ReSe<sub>2</sub> catalysts were prepared based on our previous work [28]. By varying the amount of dibenzyl diselenide, we can also obtain the sample of rhenium selenide with an appropriate concentration of selenium vacancies. The detailed process can be seen in Supplementary Material. Based on a unique and direct ultrasound-assisted stripping method, 20 mg as-obtained dry bulk ReSe<sub>2</sub> or ReSe<sub>2</sub>(SV) was added into 20 mL ethanol and treated with ultrasound for 300 min. The ultrasound probe was operated and stopped repeatedly with an interval of 2 s. In the ultrasonication process, the temperature of the dispersion was controlled below 25 °C using an ice bath. Then, the dispersion was centrifuged at 8000 RPM for 2 min to acquire the supernatant. The concentration of the as-synthesized

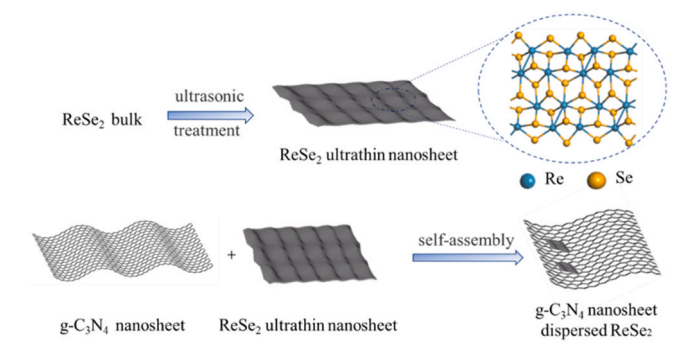


Fig. 1. Schematic diagram of the synthesis process of  $\text{ReSe}_2/\text{g-C}_3\text{N}_4$  heterojunction sample.

ReSe $_2$  and ReSe $_2$ (SV) ethanol solution was estimated to be around 20  $\mu g \ mL^{-1}$  by ICP-AES.

## 2.1.3. Fabrication of g-C<sub>3</sub>N<sub>4</sub> nanoparticles dispersed ReSe<sub>2</sub> ultrathin nanosheets (CNSR/CNSVR)

g- $C_3N_4$  (20 mg) was put into the mortar, followed by the addition of 20 mL ReSe<sub>2</sub> or ReSe<sub>2</sub>(SV) ultrathin nanosheets ethanol solution. The suspension was physically ground for 10 min. After the natural evaporation of ethanol, the solid sample was finally ground to obtain the fine powders and annealed at 250 °C for 3 h in Ar. We termed the g- $C_3N_4$ /rhenium selenide samples with and without selenium vacancies as CNSR and CNSVR, respectively. In general, the synthesis steps are schematically shown in Fig. 1.

## 2.1.4. Fabrication of g- $C_3N_4$ nanosheets dispersed bulk ReSe $_2$ (CNSR-B/CNSVR-B)

A self-assembly process with a mechanical mixing procedure was used to produce the CNSR-B and CNSVR-B composites. In the mortar, 100 mg of g- $C_3N_4$  was first added, followed by 2 mg bulk ReSe $_2$  or ReSe $_2$ (SV) samples and 50 mL ethanol. The remaining process is the same as CNSR/CNSVR.

#### 2.2. Characterization

The morphology of samples was explored on a Hitachi H7700 transmission electron microscope (TEM) and a Talos F200X (S)TEM with a spherical aberration corrector, the latter provides high resolution transmission electron microscope (HRTEM), high-angle annular dark-field scanning transmission electron microscope (HAADF-STEM) and corresponding energy-dispersive X-ray spectroscope (EDX) mapping analyses [28]. The X-ray powder diffraction (XRD) patterns were carried out on a SmartLab X'Pert powder diffractometer [28]. Electron spin resonance (ESR) analysis was performed using a JEOL-JES-FA200 to study the mechanism of the photocatalysts [28]. The Zeta potential data were measured by Malvern ZEN 3600 nanoparticles size and ZETA potential analyzer. FT-IR data were measured on a Thermo Nicolet 8700 instrument. Raman spectra were recorded on a JY-LabRamHR laser spectrometer system. The Brunauer-Emmett-Teller (BET) specific surface area and pore size distribution were derived from the N2 adsorption and desorption on a Micromeritics Tristar II 3020M analyzer [35]. The atomic force microscopic (AFM) image was acquired on the Bruker Nano Dimension Icon instrument. Elemental ratios were detected by inductively-coupled plasma atomic emission spectroscopy (ICP-AES) at Galbraith Laboratories (Knoxville, TN) [35]. Photoluminescence spectroscopy was performed on a JY Fluorolog-3-Tou steady/transient fluorescence spectrometer, and Escalab 250 XI X-ray photoelectron spectrometer (XPS) also employed on detailed band structures (XPS-VB) and spectroscopic analysis. A ZOLIX WAD-

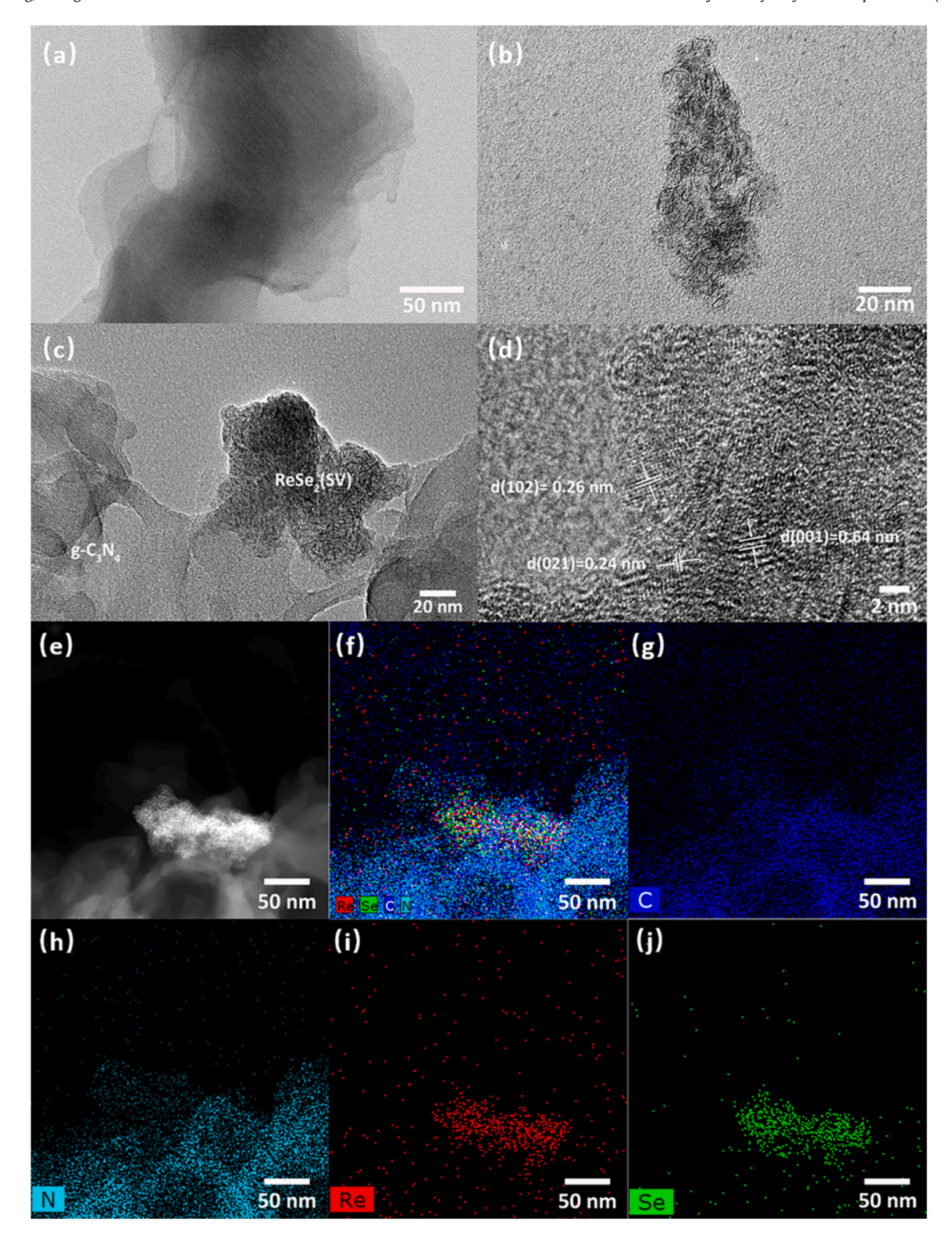


Fig. 2. TEM images of (a) g- $G_3N_4$ , (b) ReSe<sub>2</sub>(SV), (c) CNSVR, and (d) the corresponding HRTEM image of CNSVR from central area in (c), (e) STEM image and corresponding STEM-EDX elemental mapping images of (f) all elements, including (g) C, (h) N, (i) Re, and (j) Se for CNSVR.

SPV550 surface photovoltage spectrometer was used to acquire the steady-state SPV spectra.

#### 2.3. DFT calculation

All density functional theory (DFT) calculation was conducted by using Cambridge Serial Total Energy Package (CASTEP) code [29]. The

Perdew-Burke-Ernzerhof (PBE) form of the generalized-gradient approximation (GGA) function is used in the calculations [30], while OTFG ultrasoft pseudopotential and Koelling-Harmon relativistic treatment are applied [31]. The plane-wave energy cutoff is set to 408.2 eV and a Monkhorst-Pack gird parameter of  $2\times2\times1$  is adopted. During the geometry optimization task, the convergence tolerance for energy, force, stress, and displacement are set as

 $1.0 \times 10^{-5}$  eV/atom, 0.03 eV/Å, 0.05 GPa, 0.001 Å, respectively. Vacuum slabs built on the cleaved surfaces are of 10 Å to eliminate interactions between the periodic layers.

In the hydrogen evolution reaction (HER) model, an equation of  $\Delta G_{H^*} = \Delta E_{H^*} + \Delta E_{ZPE} - T\Delta S$  is used to count for the adsorption free energy of the adsorbed hydrogen atom ( $\Delta G_{H^*}$ ), where  $\Delta E_{H^*}$ ,  $\Delta E_{ZPE}$ ,  $\Delta S$ , and T stand for the hydrogen adsorption energy, the zero-point energy change in the process of hydrogen atom adsorption, the entropy variation between the adsorbed and the gas phase and room temperature (298 K), respectively. Hydrogen adsorption energy ( $\Delta E_{H^*}$ ) is defined as  $\Delta E_{H^*} = E_{cat\text{-}ad} - (0.5E_{H_2} + E_{cat})$ , where  $E_{cat}$  is the final enthalpy of the isolated surface,  $E_{cat\text{-}ad}$  is the final enthalpy of the adsorbed surface and  $E_{H_2}$  is the final enthalpy of an isolated hydrogen molecule.  $\Delta E_{ZPE}$  is 0.11 eV [28]. Since vibrational entropy in the adsorbed state is so small that can be ignored, T $\Delta S$  can be calculated by T $\Delta S = -0.5$  T $\Delta S_{H_2} = -0.205$  eV, in which  $\Delta S_{H_2}$  stands for the entropy of hydrogen molecule in the gas phase at standard conditions [32].

#### 2.4. Photoelectrochemical measurements

The photoelectrochemical properties of the samples were identified with a CHI 770E electrochemical workstation made in China by built a classical three-electrode system. Specifically, 3 mg of sample was dispersed in 2 mL hexane by ultrasonic treatment to get slurry. Then, the working electrode was prepared by dropping the slurry onto a precleaned fluoride tin oxide (FTO) glass and then dried at room temperature. A platinum electrode was utilized as the counter electrode, and Saturated Calomel Electrode (SCE) electrode was employed as the reference electrode [35]. 0.5 M Na<sub>2</sub>SO<sub>4</sub> solution was used as electrolyte. During the experiment, a 300 W Xe lamp with a  $\lambda \ge 420 \, \text{nm}$  cut filter was used to simulate a visible light environment. The Electrochemical impedance spectroscopy (EIS) was performed at open circuit voltage in the frequency range 100 kHz to 0.1 Hz [36]. The transient photocurrent responses of the samples were tested in a bias of 1.0 V vs. SCE under the same light conditions. The Mott-Schottky plots were measured at the frequency of 1000 Hz in impedance potential mode.

#### 2.5. Photocatalytic hydrogen production

20 mg catalyst samples were ultrasonically dispersed in 20 mL triethanolamine solution (15 vol%). Then, the solution was transferred to photocatalytic reactor, and argon is introduced to replace the air in the reactor. A 300 W Xe lamp with a  $\lambda\!\geq\!420$  nm cut filter was used to simulate a visible light environment, the headspace gas (ca. 50 mL) of the reactor was sampled (500  $\mu L$  per sample) every 60 min, injecting the sample into the calibrated gas chromatograph to detect the amount of  $H_2$ .

#### 3. Results and discussion

#### 3.1. Morphology and structure characterization

The morphologies of the as-prepared samples were studied using HRTEM determinations.  $g\text{-}C_3N_4$  shows a typical hierarchical structure, and the massive rhenium selenide shows a flower-like structure [28]. The introduction of selenium vacancies reduced the crystallinity of rhenium selenid and the formation of dense aggregated states in nanomaterials (Fig. 2a, S1a and S1b). Fig. 2b–d illustrate the rhenium selenide ultrathin nanosheets with selenium vacancies after sonication, showing successful self-assembly with  $g\text{-}C_3N_4$  nanosheets. The interlayer gap of 0.64 nm in the HRTEM image indicates the lattice distance of (001).

facets in triclinic ReSe<sub>2</sub> (JCPDS No. 01-074-0611). Meanwhile, the XRD patterns of the as-synthesized 1T phase rhenium selenide

samples exhibit broadened diffraction characteristics (Fig. S2), which is consistent with the poor crystallinity exhibited in the electron microscopic tests. Furthermore, the EDS elemental mappings of CNSVR and ReSe<sub>2</sub>(SV) were performed, which shows that the C, N, Re, and Se elements were dispersed throughout CNSVR samples, indicating a significant interaction between ReSe<sub>2</sub>(SV) nanosheets and g-C<sub>3</sub>N<sub>4</sub> (Fig. 2e-j and S1c-f).

To further demonstrate the successful combination of the nanosheets, we performed the zeta potential of the g-C<sub>3</sub>N<sub>4</sub>, ReSe<sub>2</sub>(SV) and CNSVR nanosheets under different conditions. As shown in Fig. S3, pH = 7 is the environment, under which  $g-C_3N_4$  nanosheets and ReSe<sub>2</sub>(SV) nanosheets were compounded to form CNSVR nanosheets. pH = 10 is the photocatalytic working environment (triethanolamine as sacrificial agent). The ReSe<sub>2</sub>(SV) nanosheets show a positive zeta potential of 12.3 mV at pH = 7, whereas the  $g-C_3N_4$ nanosheets exhibit a negative zeta potential of -29.3 mV at the same pH value. The opposite zeta potentials result in strong electrostatic attraction between ReSe<sub>2</sub>(SV) nanosheets and g-C<sub>3</sub>N<sub>4</sub> nanosheets [37,38]. It is found that zeta potential of the CNSVR obtained composite is -16.9 mV, intermediate between the two individual nanosheets. Thus, stable 2D/2D ReSe<sub>2</sub>(SV)/g-C<sub>3</sub>N<sub>4</sub> heterojunctions can be obtained by the Coulomb electrostatic interaction, and the stability of the material was subsequently strengthened by annealing. Under alkaline conditions (pH = 10), all three kinds of nanosheets exhibited negative potentials, where the zeta potential of g-C<sub>3</sub>N<sub>4</sub> nanosheets is -48.1 mV, the zeta potential of ReSe<sub>2</sub>(SV) nanosheets is -26.6 mV, and the zeta potential of CNSVR nanosheets is -40.8 mV. As a result, the Zeta potential value of the composite is still between the ones of the two individual nanosheets. The absolute value of zeta potential increases for all the three nanosheets under the same varied condition, suggesting that the nanosheets are more stable and less likely to agglomerate under alkaline conditions [37,38].

XRD was used to analyze the crystal structures of the samples. The patterns of g-C<sub>3</sub>N<sub>4</sub>, CNSR, CNSR-B, CNSVR, and CNSVR-B are shown in Fig. 3a. Due to its high dispersion and low loading concentration, the hybrids do not have any identifiable diffraction peaks of ReSe<sub>2</sub>. Meanwhile, EPR measurements confirmed the presence of selenium vacancies within the ReSe<sub>2</sub>(SV) nanosheets, which are typically paramagnetic defects in semiconductors. The EPR signal for ReSe<sub>2</sub>(SV) nanosheets at  $g_{iso} = 2.0012$  (close to the free-electron value,  $g_e = 2.0023$ ) could be well referred to the selenium vacancies, while the ReSe2 nanosheets at the same location show a lower signal, which clearly indicates that ReSe<sub>2</sub>(SV) nanosheets have a higher concentration of selenium vacancies, as seen in Fig. 3b [27,28,33]. Fig. 3c shows that  $g-C_3N_4$  and all  $ReSe_2/g-C_3N_4$  samples exhibit identical FT-IR characteristic signals. The strong bands extending from 1100 to 1700 cm<sup>-1</sup> correspond to the stretching vibrations of aromatic C-N heterocycles, while the large peaks between 3000 and 3500 cm<sup>-1</sup> are attributed to O-H and N-H vibrations. The signal of the tri-s-triazine unit has maxima at 810 cm<sup>-1</sup>. This study shows that following the self-assembly process, the g-C<sub>3</sub>N<sub>4</sub> retains its primary structure [34,35]. In Fig. S4, we compared the Raman spectra of g-C<sub>3</sub>N<sub>4</sub> and CNSVR under 1064 nm excitation, the peaks at 711 cm<sup>-1</sup> (Heptazine ring breathing modes) and 763 cm<sup>-1</sup> are originated from A1' mode of g-C<sub>3</sub>N<sub>4</sub>, and the peaks at 1233 cm<sup>-1</sup> (typical stretching vibration modes of C=N and C-N heterocycles) and 1311 cm<sup>-1</sup> (semi-circle stretching) are derived from E' mode of g-C<sub>3</sub>N<sub>4</sub> [39]. Compared to pure g-C<sub>3</sub>N<sub>4</sub>, a new characteristic peak can be detected near 145 cm<sup>-1</sup> of the CNSVR sample, derived from the complex manifold of intralayer modes of ReSe<sub>2</sub> samples [25,26]. BET analysis was also used to investigate the physicochemical information of g-C<sub>3</sub>N<sub>4</sub>, CNSVR-B and CNSVR, as shown in Fig. 3d and Table S1. The specific surface area of g-C<sub>3</sub>N<sub>4</sub> increased dramatically after grinding and dispersion treatment, from  $81.20 \text{ m}^2 \text{ g}^{-1}$  in g-C<sub>3</sub>N<sub>4</sub> to  $173.29 \text{ m}^2 \text{ g}^{-1}$  in CNSVR-B. In general, photocatalysts with the increased specific surface area might give

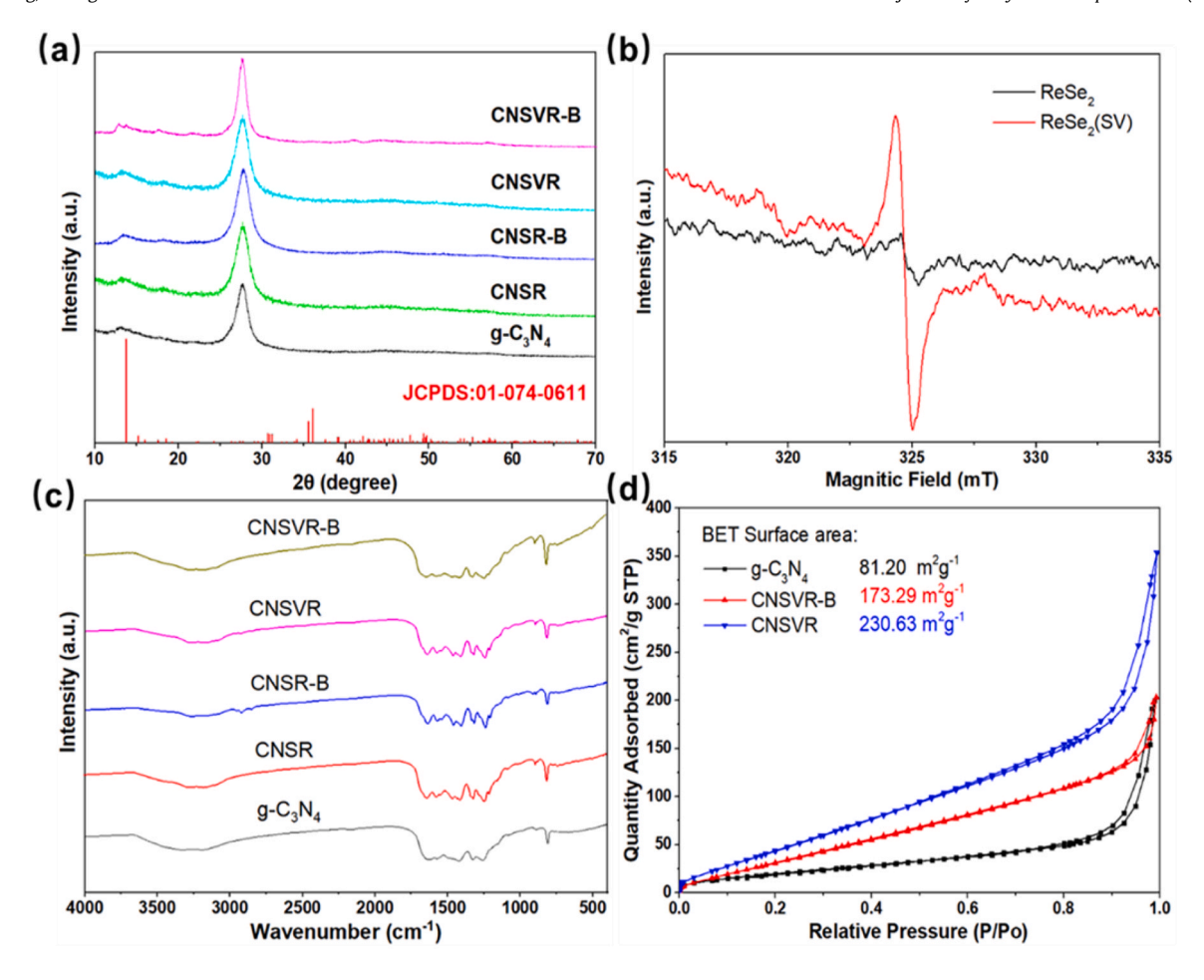


Fig. 3. (a) XRD patterns of g- $C_3N_4$  and  $ReSe_2/g$ - $C_3N_4$  heterojunctions, (b) EPR spectra of  $ReSe_2$  and  $ReSe_2(SV)$  samples, (c) FT-IR patterns of g- $C_3N_4$  and  $ReSe_2/g$ - $C_3N_4$  heterojunctions, and (d)  $N_2$  adsorption–desorption isotherms of g- $C_3N_4$ , CNSVR-B and CNSVR samples.

more surface reactive sites while also improve light absorption, making photocatalysis easier. Besides, the CNSVR sample even has a larger surface area  $(230.63 \,\mathrm{m^2 \ g^{-1}})$  than CNSVR-B has, which suggests that better dispersion of ReSe<sub>2</sub> ultrathin nanosheets on the g-C<sub>3</sub>N<sub>4</sub> surface leads to a larger surface area. Furthermore, the huge surface area of ReSe<sub>2</sub> ultrathin nanosheets results in more exposed reactive sites on g-C<sub>3</sub>N<sub>4</sub>, which results in higher photocatalytic activity of CNSVR as compared with CNSVR-B [21,35].

To further understand the critical function of the atomic-level edge active sites of ReSe2 ultrathin nanosheets, we examined AFM images of bulk ReSe<sub>2</sub>(SV) samples, large-size ReSe<sub>2</sub>(SV) nanosheets, and ultrathin ReSe<sub>2</sub>(SV) nanosheets, where the large- size ReSe<sub>2</sub>(SV) nanosheets are obtained by dispersion of bulk ReSe<sub>2</sub>(SV) after ball milling. The bulk ReSe<sub>2</sub>(SV) has the biggest lateral dimension of ~5 µm and thickness of 1.08 µm among them (Fig. 4a, d). The largesize ReSe<sub>2</sub>(SV) nanosheets have a lateral diameter of ~300 nm and a thickness of 33.50 nm (Fig. 4 b, e). Ultrathin ReSe<sub>2</sub>(SV) nanosheets, on the other hand, have a lateral dimension of ~250 nm and the thinnest thickness of 4.89 nm (Fig. 4c, f). The ultrasonication procedure resulted in ReSe2 ultrathin nanosheets with reduced thickness and more accessible edge sites. For hydrogen evolution, ReSe<sub>2</sub>(SV) nanosheets with smaller lateral diameters have more exposed edge active sites [21]. Furthermore, because of the interlayer decoupling property of ReSe<sub>2</sub>(SV), thinner ReSe<sub>2</sub>(SV) nanosheets possess a greater interface and better electronic coupling with g-C<sub>3</sub>N<sub>4</sub> nanosheets, ensuing more effective charge carrier separation and transferring. These results were also validated by the following DFT calculations.

#### 3.2. DFT model establishment and calculations

According to the morphological studies in our calculations, the ultrathin ReSe2 nanosheets were simulated as single-layer ReSe2, and extend infinitely in the lateral dimension. We intercepted part of 4 × 4 molecule to make a schematic diagram, in which each diagram consisted of 16 Re atoms and 32 Se atoms. On six distinct types of sites, we calculated the Gibbs free energy of hydrogen adsorption. As shown in Fig. 5, Fig. S5 and Table S2, on the basal S1, S2, S3 and S4 Se sites (Fig. S5a-d), the Gibbs free energies of hydrogen adsorption are 1.24, 1.37, 0.45 and 0.77 eV, respectively (Table S2). These generally positive results suggest that hydrogen atoms have a great difficulty adsorbing on the aforementioned basal Se sites, exposing the low hydrogen evolution activities on the Se sites in the base surface of ReSe<sub>2</sub> monolayer. Correspondingly, the functions of hydrogen evolution on the edge sites of ReSe2 ultrathin nanosheets were also investigated. As a result, the Gibbs free energies for hydrogen adsorption on the edge S1 and edge S2 Se sites (Fig. 5b, c) were estimated as -0.16 and 0.29 eV, respectively (Table S2). Comparison of all sites are illustrated in Gibbs free energy diagram of HER (Fig. 5a), the  $\Delta G_{H^*}$  value for the edge Se sites is much closer to the ideal  $\Delta G_{H^*}$ , in particular, the edge S1 site, which is very close to zero and perfect for HER. Theoretically, based on the studies of the preceding calculations, the non-saturated coordination Se site can be operated as the center of the HER. Meanwhile, the ultrathin ReSe<sub>2</sub> nanosheets appear to be essentially intact plane. Although the internal sites in the basal plane are unfavorable candidate for the HER reaction site, it could be served as an ideal platform for electron migration, allowing electrons to reach these peripheral active sites [21,28].

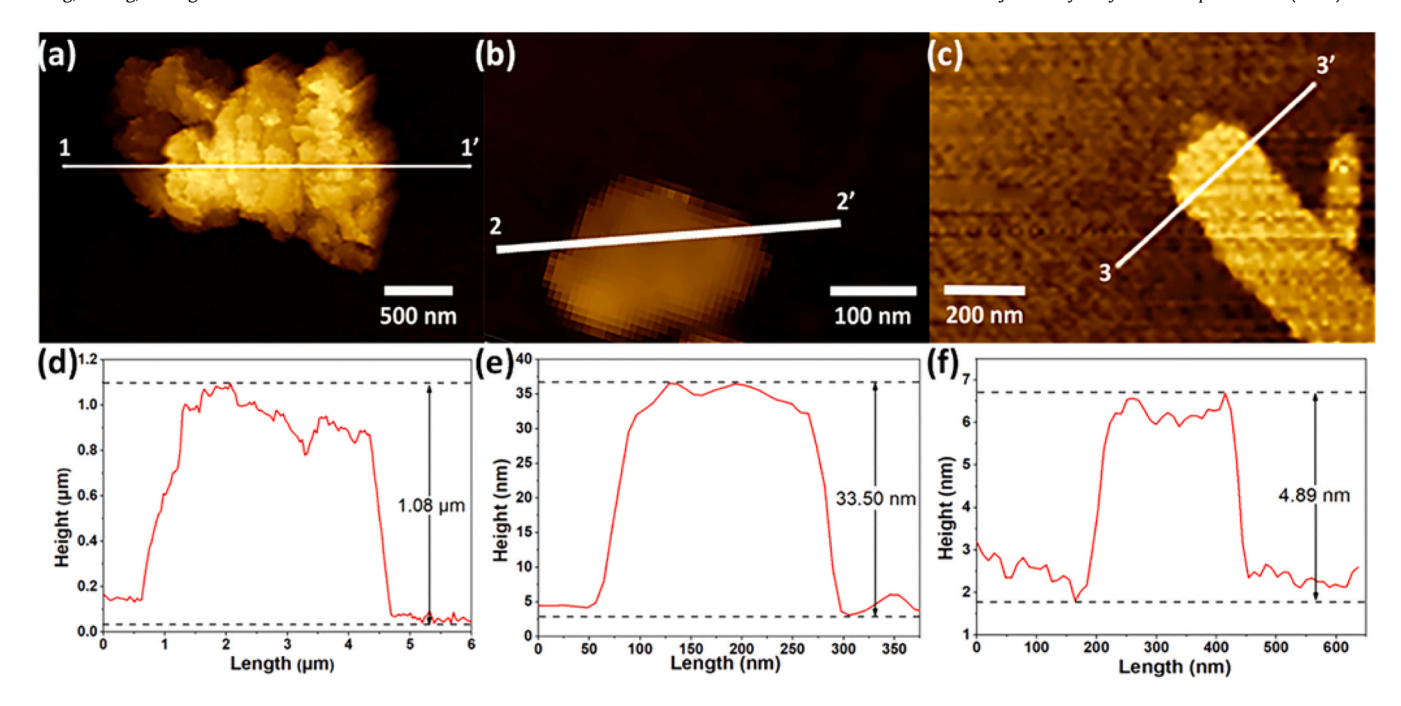
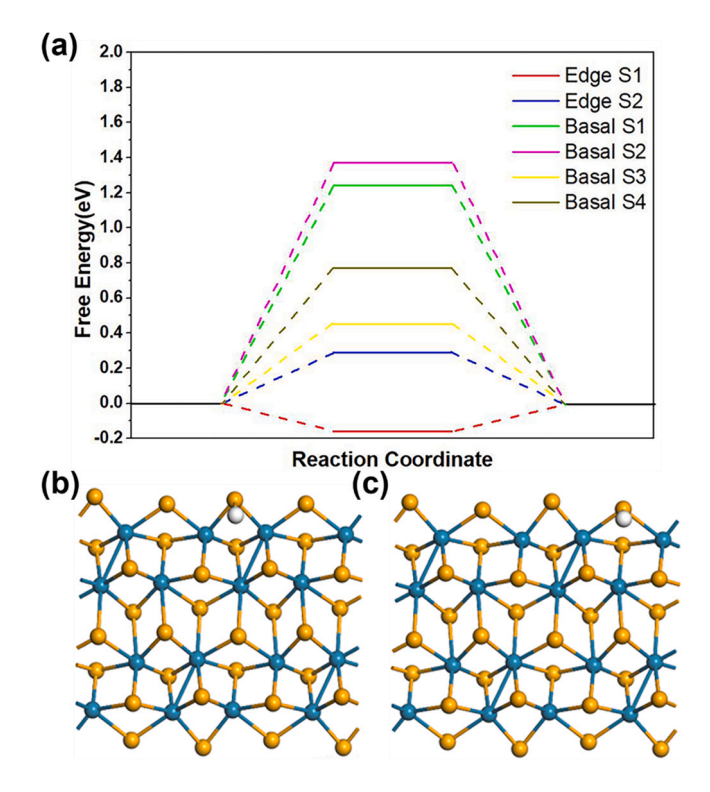


Fig. 4. AFM images of (a) bulk ReSe<sub>2</sub>(SV), (b) large-size ReSe<sub>2</sub>(SV) nanosheet, and (c) ultrathin ReSe<sub>2</sub>(SV) nanosheets and their corresponding height profiles of (d) bulk ReSe<sub>2</sub>(SV), (e) large-size ReSe<sub>2</sub>(SV) nanosheet, and (f) ultrathin ReSe<sub>2</sub>(SV).



**Fig. 5.** (a) Gibbs free energy diagram of HER on the Se sites of ReSe<sub>2</sub>. Atomic structures (top view) of hydrogen adsorption on (b) Edge S1, and (c) Edge S2 sites of ReSe<sub>2</sub>. The blue, yellow and white spheres are used to represent Re, Se and H atoms, respectively.

#### 3.3. XPS analysis

X-ray photoelectron spectroscopy (XPS) was used to examine the chemical binding states of photocatalyst composites. Both ReSe<sub>2</sub> and ReSe<sub>2</sub>(SV) include Re and Se elements in their XPS survey spectra

(Fig. S6a), which is consistent well with the EDS-mapping finding. The C 1s signal for the ReSe<sub>2</sub> and ReSe<sub>2</sub>(SV) samples is standardized identically at 284.8 eV in Fig. S6b. The binding energies at 43.9 and 41.5 eV for the ReSe<sub>2</sub> samples are attributed to Re  $4f_{5/2}$  and Re  $4f_{7/2}$ , respectively, while peaks at 54.65 and 55.45 eV are accessed to Se  $3d_{5/2}$  and Se  $3d_{3/2}$ , respectively [25–28]. The peak at 45.7 eV should be originated from the high-valent state Re in the minority unreacted NH<sub>4</sub>ReO<sub>4</sub>, which can be easily dissolved in ethanol and thus washed away during the ultrasound process, so we can see that the peak around 45.7 eV in the CNSVR composite almost disappears. However, the binding energies of Re 4f and Se 3d in the ReSe<sub>2</sub>(SV) sample increased by 0.10 eV (Fig. S6c, d). This trend toward higher binding energies is consistent with the earlier findings in comparable circumstances of WSe<sub>2</sub> samples [33,40,41], the Fermi level edges are closer to the boundary of conduction band. We also used ICP-AES to determine the elemental molar ratios in the ReSe2 and ReSe<sub>2</sub>(SV) samples, as described in Table S3. The Se concentration of the ReSe<sub>2</sub>(SV) samples is lower than that of the ReSe<sub>2</sub> samples, indicating that selenium vacancies exist in the ReSe<sub>2</sub>(SV) samples and correlating with the EPR finding [25-28,33].

The chemical states of elements were then investigated before and after the dispersion and loading of ReSe2(SV) ultrathin nanosheets in g-C<sub>3</sub>N<sub>4</sub>. In C 1s spectra (Fig. 6a), two peaks for g-C<sub>3</sub>N<sub>4</sub> are detected with binding energies of 284.8 and 288.25 eV. In detail, the peak at 284.8 eV binding energies is attributed to adventitious C, and the sp<sup>2</sup>-hybridized carbon (N-C=N) is responsible for the binding energy maxima at 288.25 eV. C 1s spectra from CNSVR also show two peaks emanating from C with binding energy locations nearly equal to g-C<sub>3</sub>N<sub>4</sub>. Fig. 6b displayed the N 1s spectra of the g-C<sub>3</sub>N<sub>4</sub> samples, three peaks confirm the existence of C-N=C at 398.80 eV, N-C<sub>3</sub> at 400.05 eV, and N-H at 401.33 eV, respectively. By contrast, the N-C<sub>3</sub> and N-H peaks of CNSVR are extended to higher binding energies of 0.29 and 0.17 eV, accordingly. In conversely to N 1s spectra, all CNSVR peaks in Re 4f and Se 3d spectra have a negative energy shift as compared to bulk ReSe<sub>2</sub>(SV) samples, which apparently indicates the transfer of electrons from the g-C<sub>3</sub>N<sub>4</sub> to ReSe<sub>2</sub>(SV) (Fig. 6c, d). In short, the extensive contacts between ReSe<sub>2</sub>(SV) and g-C<sub>3</sub>N<sub>4</sub> are proven by the shifts in binding energies in CNSVR

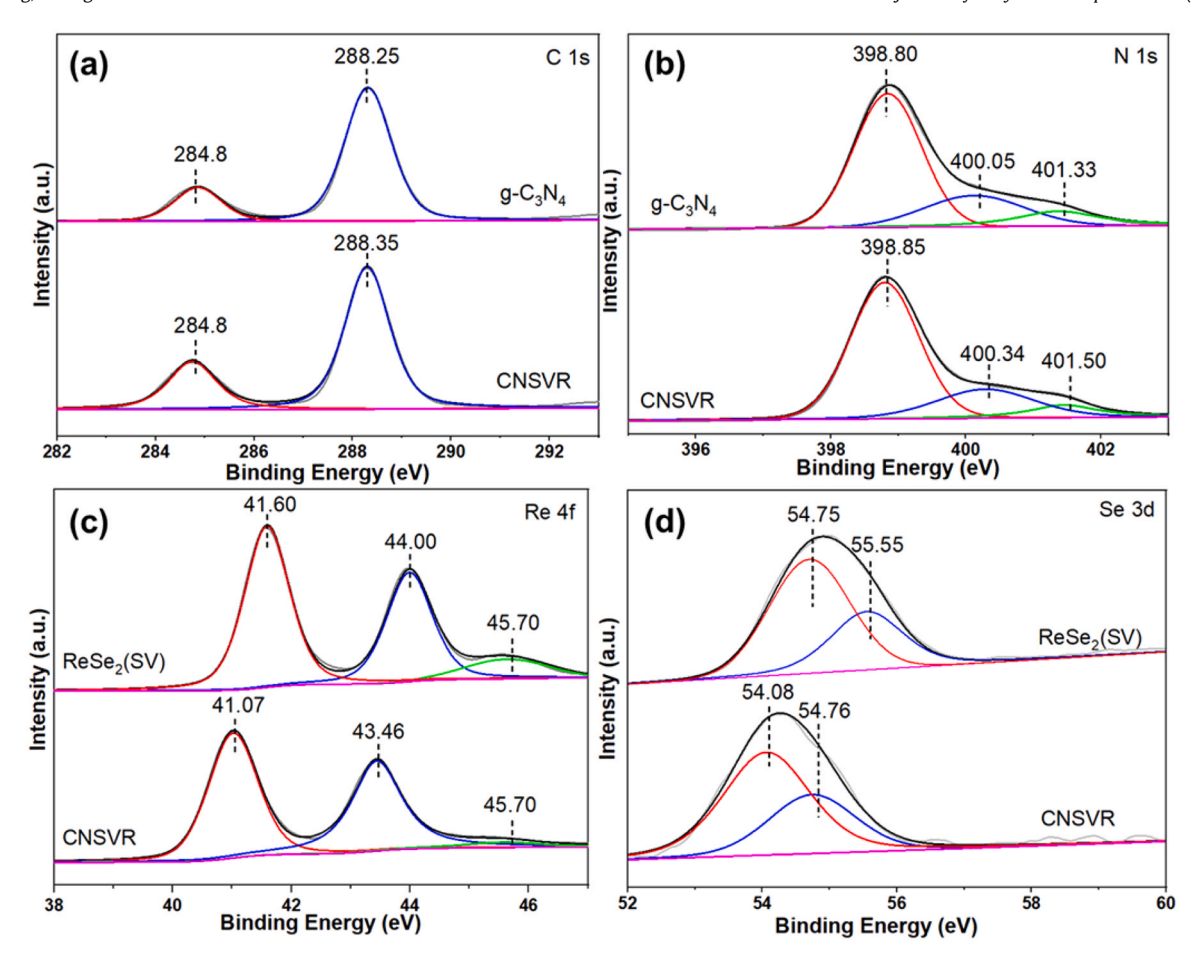


Fig. 6. Comparison of HR-XPS before and after dispersion and loading ReSe<sub>2</sub>(SV) ultrathin nanosheets on g-C<sub>3</sub>N<sub>4</sub> nanoparticles: (a) C 1s, (b) N 1s, (c) Re 4f, and (d) Se 3d.

composites, demonstrating that  $ReSe_2(SV)$  has been dispersed on g- $C_3N_4$  to form heterojunction [27,35,42,43].

#### 3.4. Optical measurement and bandgap analysis

UV-Vis diffuse reflection spectra were used to study the optical absorption characteristics of the performed materials. Fig. 7a demonstrates that bare g-C<sub>3</sub>N<sub>4</sub> has a strong absorption intensity in the ultraviolet region, while a mild absorption in the visible area ( $\lambda$  > 420 nm). Due to the quantum size effect generated by the ultrasonic self-assembly process and the color of g-C<sub>3</sub>N<sub>4</sub> changed from light yellow to gray as a result of the loading, the absorption capacity and absorption range of the g-C<sub>3</sub>N<sub>4</sub> samples loaded with ReSe<sub>2</sub> was improved in the visible region as compared to bare g-C<sub>3</sub>N<sub>4</sub>. The Tauc plot was used to determine the bandgap energy of the bare g-C<sub>3</sub>N<sub>4</sub>, ReSe<sub>2</sub>(SV) ultrathin nanosheets and ReSe<sub>2</sub> ultrathin nanosheets as illustrated in Fig. 7b. As a result, the bandgap energies for g-C<sub>3</sub>N<sub>4</sub>, ReSe<sub>2</sub>(SV) ultrathin nanosheets and ReSe<sub>2</sub> ultrathin nanosheets were estimated to be 2.93, 1.24 and 1.28 eV, respectively. The introduction of a modicum of selenium vacancies results in a slight reduction of the bandgap, which is due to the modification of the electronic structure by the vacancies and can help to improve the HER performance of ReSe<sub>2</sub> nanosheets according to our previous report and calculation in electrochemical work [28]. Meanwhile, the previous report indicated the band gap of rhenium selenide nanosheets is related to its number of layers, the decrease of the layers leads to the band gap wider [44]. Fig. S7 shows the calculated results of the density of states (DOS) for bulk and monolayer ReSe2, and the band gap of 1.24 eV is close to that of single-layer nanosheets, which is consistent with the previous morphological analysis. To acquire

information on the conduction band (CB) and valence band (VB) locations, Mott Schottky plots were measured in Fig. 7c, g-C<sub>3</sub>N<sub>4</sub>, ReSe<sub>2</sub> ultrathin nanosheets and ReSe<sub>2</sub>(SV) ultrathin nanosheets all show typical n-type semiconductor characteristics and g-C<sub>3</sub>N<sub>4</sub>, and ReSe<sub>2</sub>(SV) ultrathin nanosheets had E<sub>CB</sub> of -0.97 and -0.36 V, respectively. Combined with the band gap, we can calculate the E<sub>VB</sub> of g-C<sub>3</sub>N<sub>4</sub> and ReSe<sub>2</sub>(SV) ultrathin nanosheets, which are 1.96 and 0.88 V, respectively. The XPS-VB experiment is also used to verify this conclusion, and the E<sub>VB. XPS</sub> of g-C<sub>3</sub>N<sub>4</sub> and ultrathin ReSe<sub>2</sub>(SV) has been characterized to be 1.90 and 0.82 V, respectively (Fig. 7d, e). The valence bands of the two samples were calculated according to the following equation:  $E_{VB, NHE} = \varphi + E_{VB, XPS} - 4.44$ , where  $\varphi$  is the work function of the XPS instrument (4.5 eV) [45]. Consequently, the EVB. NHE of g-C<sub>3</sub>N<sub>4</sub> and ultrathin ReSe<sub>2</sub>(SV) is calculated to be 1.96 and 0.88 V, which is consistent with the results estimated by electrochemical methods. As revealed in the above band gap analysis, the ultrathin ReSe<sub>2</sub>(SV), as a co-catalyst, forms a heterojunction with g-C<sub>3</sub>N<sub>4</sub>, and the energy band structure information was provided in Fig. 7f.

#### 3.5. Photocatalytic hydrogen evolution

Fig. 8a summarizes the hydrogen yields of different samples in the similar photocatalytic environment. The hydrogen production rate of bare g-C<sub>3</sub>N<sub>4</sub> as a control group was 50.18  $\mu$ mol g<sup>-1</sup> h<sup>-1</sup>. The hydrogen production rates of CNSR-B and CNSVR-B samples obtained by mechanical mixing of bulk ReSe<sub>2</sub> and ReSe<sub>2</sub>(SV) dispersed in g-C<sub>3</sub>N<sub>4</sub> were slightly increase to 100.03 and 155.96  $\mu$ mol g<sup>-1</sup> h<sup>-1</sup> while the hydrogen production rates of CNSR and CNSVR samples acquired by ultrasonic ultrathin nanosheets dispersed in g-C<sub>3</sub>N<sub>4</sub>

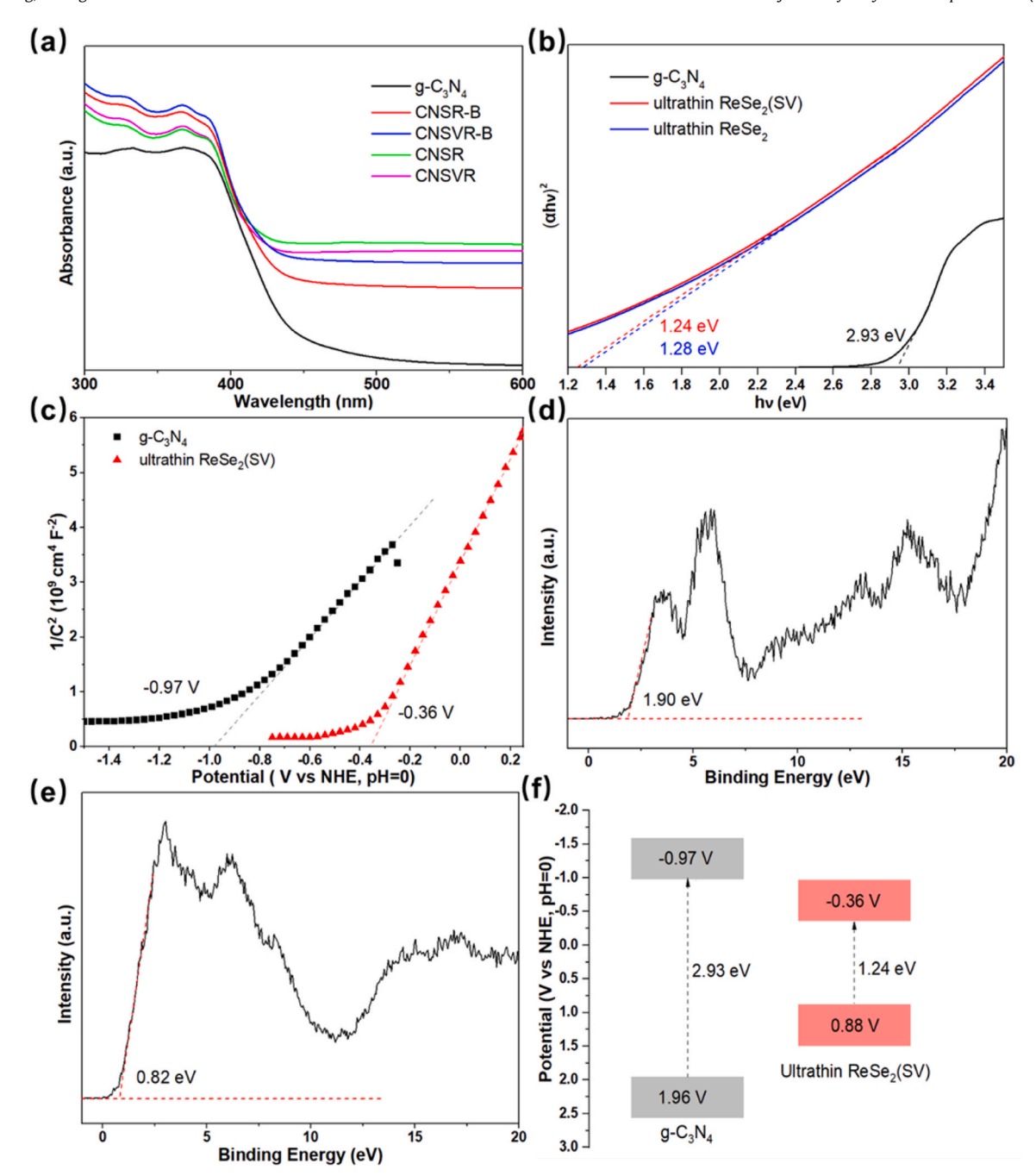


**Fig. 7.** (a) UV-Vis (DRS) spectra of  $C_3N_4/ReSe_2$  samples, (b) Tauc plots, and (c) Mott-Schottky plots of single semiconductor, using 0.5 M sodium sulfate as electrolyte solution; XPS-VB of (d)  $g-C_3N_4$ , and (e) ultrathin  $ReSe_2(SV)$  samples, and (f) band structure diagrams of  $g-C_3N_4$  and ultrathin  $ReSe_2(SV)$  samples.

were 765.15 and 1055.50  $\mu$ mol g<sup>-1</sup> h<sup>-1</sup>, respectively. Increased active sites and efficient charge transfer due to the dispersion and loading of ReSe<sub>2</sub> are responsible for the dramatic rise in photocatalytic activity, and the two-dimensionalization of ReSe<sub>2</sub> by ultrasonic process plays a key role in the photocatalytic performances. In Fig. S8, the detected results proved that triethanolamine is the best sacrificial agent. For alcohols, their oxidation potentials are all higher than that of triethanolamine (TEOA), the lack of hydrophilic on the g-C<sub>3</sub>N<sub>4</sub> surface makes alcohols more difficult to be adsorbed on g-C<sub>3</sub>N<sub>4</sub> surfaces [46,47]. These factors resulted in alcohols being far less effective as sacrificial agents as compared to TEOA. For Na<sub>2</sub>S, its oxidation potential is lower than TEOA, which can better protect TMDs from photocorrosion [48]. However, our supplementary experimental results were more similar to pure g-C<sub>3</sub>N<sub>4</sub> sample, the

 $g-C_3N_4$  amine groups are protected by the presence of TEOA, thus the catalytic performance is superior to that of  $Na_2S$  when TEOA is used as a sacrificial agent. It is concluded that the above results imply that most of the photogenerated holes and sacrificial agents react on the  $g-C_3N_4$  surface [49,50].

On the other hand, it is proved that the introduction of selenium vacancies based on the self-assembly process can further enhance the photocatalytic performance. Additionally, the impact of the quantity of loading ultrathin nanosheets was studied, as shown in Fig. S9. The results suggest that a 2 % mass fraction loading, i.e. invest 20 mL of ReSe<sub>2</sub>(SV) ultrathin nanosheets ethanol solution to synthesize CNSVR, provides the finest catalytic effect. When the quantity of loading was further increased, overloading ReSe<sub>2</sub> nanosheets lead to the coverage of the active sites on the surface and the

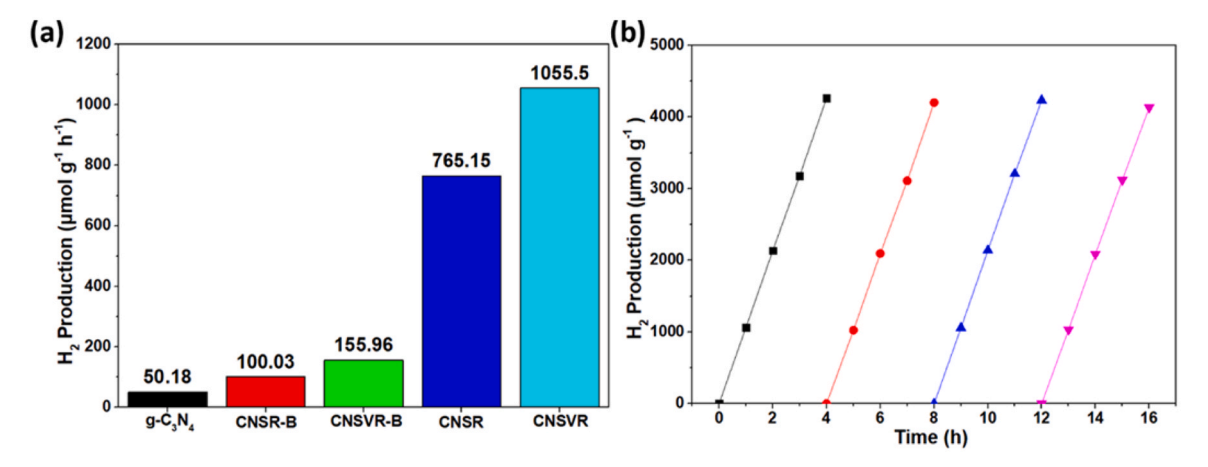


Fig. 8. (a) Photocatalytic  $H_2$  production rates of g- $C_3N_4$ , CNSR-B, CNSVR-B, CNSR and CNSVR photocatalyts ( $\lambda \ge 420$  nm), and (b) photocatalytic stability experiment results of CNSVR for repetitive  $H_2$  evolution reactions ( $4 \times 4$  h cycles, exhausting the gas from the reactor every 4 h and restarting hydrogen collection).

blocking of the incident light. Based on this optimal catalyst, we further tested the external quantum yield (EQY) of the sample at several different wavelengths (See in Table S4 for specific calculation details) [51]. Similar to the light absorbance capacity of g-C<sub>3</sub>N<sub>4</sub> at different wavelengths, the EQY of the CNSVR sample in the visible light region at 420 nm was 5.38 %. While in the UV region 365 nm and 400 nm, the CNSVR sample achieved higher EQY results of 12.82 % and 10.71 %, respectively. This phenomenon shows that the catalyst still conforms to the general properties of g-C<sub>3</sub>N<sub>4</sub> based materials. Furthermore, in Fig. 8b, 4 × 4h repetitive tests were used to assess the photocatalytic stability of CNSVR sample. The photocatalytic hydrogen evolution rate of a CNSVR sample did not vary significantly in last 16 h. Before and after the photocatalysis reaction, the XRD, FT-IR and XPS investigations revealed that every distinctive peak location did not vary appreciably (See supplementary material Figs. S10-S12), and the HRTEM images of CNSVR after the reaction (Figs. S13a, b) are not significantly different from the Morphologic images before the reaction (Fig. 2c, d), thus the stability of the Re-Se<sub>2</sub>(SV)/g-C<sub>3</sub>N<sub>4</sub> combination was determined by these characterization data. ReSe<sub>2</sub>(SV) composites display a significantly high photocatalytic hydrogen evolution rate when compared to other conventional g-C<sub>3</sub>N<sub>4</sub>-based heterojunction photocatalysts, indicating that ReSe<sub>2</sub> might be a promising efficient cocatalyst to boost the semiconductor's photocatalytic activity. Combining the previous data, the ReSe<sub>2</sub>(SV) composites showed a very significant improvement for the photocatalytic hydrogen rate.

To evaluate the photocatalytic activity objectively, a comparison of the photocatalytic performance of the present work with the early work using some g-C<sub>3</sub>N<sub>4</sub>-based type II [52-54], Z-scheme [55-58] and S-scheme [46,59,60] heterojunctions as catalysts are presented in Table S5. As noted, similar heterostructured strategy has been applied for electrocatalytic hydrogen production although they have different redox reaction driving ways [28,61-63]. In the present work, the CNSVR nanosheets did not perform as good as many Zscheme or S-scheme heterojunctions while they are still show higher activities comparing with lots of type II heterojunctions, especially without addition of Pt or other co-catalysts. The high performance of the g-C<sub>3</sub>N<sub>4</sub>/ReSe<sub>2</sub> nanosheets is attributed to the fact that ReSe<sub>2</sub> nanosheets similarly serving as a co-catalyst plays a key role in the improvement of the photocatalytic reactivity since most of the photogenerated holes on the g-C<sub>3</sub>N<sub>4</sub> surface are not transferred but directly consumed by the sacrificial agent [64–66]. This phenomenon suggests that the as-designed g-C<sub>3</sub>N<sub>4</sub>/ReSe<sub>2</sub> nanosheets still have some unique advantages in terms of significantly increased edge active sites and developing noble metal-free catalytic systems.

#### 3.6. Photoelectrochemical performance and electron transfer discussion

To investigate the impact of active sites and vacancies on HER catalytic activity, electrochemical impedance spectroscopic (EIS) measurements were used to look at the kinetic resistance of charge transfer. The resultant Nyquist plots (Fig. 9a, Table S6) indicated that the CNSVR sample had the lowest semicircular diameter of all the examined materials, indicating that it has a better interface reaction than other g-C<sub>3</sub>N<sub>4</sub>/ReSe<sub>2</sub> heterojunctions. As illustrated in Fig. 9b, under visible light illumination, all as-prepared samples showed repeatable photocurrent density, and the addition of co-catalyst ReSe<sub>2</sub> makes the photocurrent response intensity increase. The photocurrent responses of CNSVR sample have the maximum photocurrent density in light on/off cycles. To further investigate the kinetics of electron transfer between catalysts, we selected the bare g-C<sub>3</sub>N<sub>4</sub> for some comparison experiments with the best catalytic sample CNSVR. The steady-state photoluminescence (PL) pattern at 345 nm excitation (Fig. 9c) showed that g-C<sub>3</sub>N<sub>4</sub> gives a broad band centered at ~480 nm, while the peak of the composite CNSVR is blueshifted to near 445 nm and its intensity is significantly decrease. The reduction of photoluminescence signal intensity in the CNSVR suggests that electron transfer is most effective in the composites, while the peak blueshift is due to quantum restriction effects induced by the ultrasonic dispersion and self-assembly process [67,68]. Moreover, consistent with steady-state PL data, the corresponding transient fluorescence curves were collected at the same 365 nm emission peak, as shown in Fig. 9d. The three radiative lifetimes  $(\tau_1 - \tau_3)$ , as well as the average radiative lifespan  $(\tau_{ave})$  of CNSVR, are drastically decreased when compared to bare g-C<sub>3</sub>N<sub>4</sub>. These multiple time constants are derived from charge transfer, various trapping processes and/or intrinsic lifetime heterogeneity. Thus, the fact that the average relaxation lifetime of CNSVR is shorter than that of bare g-C<sub>3</sub>N<sub>4</sub> suggests that charge transfer on CNSVR surface is more efficient, which also explains the higher photocatalytic activity of CNSVR in agreement [69]. The results of the steady-state surface photovoltage (SPV) spectra (Fig. 9e) show that the SPV values of CNSVR are much larger than those of bare g-C<sub>3</sub>N<sub>4</sub>. It revealed that more photo-induced electron-hole pairs are transferred to the surface of CNSVR, the introduction of ReSe<sub>2</sub>(SV) ultrathin nanosheets and the formation of heterojunctions can enhance the separation efficiency of the g-C<sub>3</sub>N<sub>4</sub> surface effectively. The unpaired electrons in the samples were also investigated using EPR with visible light irradiation. Fig. 9f shows that each sample has a single Lorentzian line centered at  $g_{iso}$  = 2.0013 (close to the free-electron value,  $g_e$  = 2.0023), which corresponds to the produced conduction electrons in the confined  $\pi$  system of g-C<sub>3</sub>N<sub>4</sub> system [70]. The heterojunction

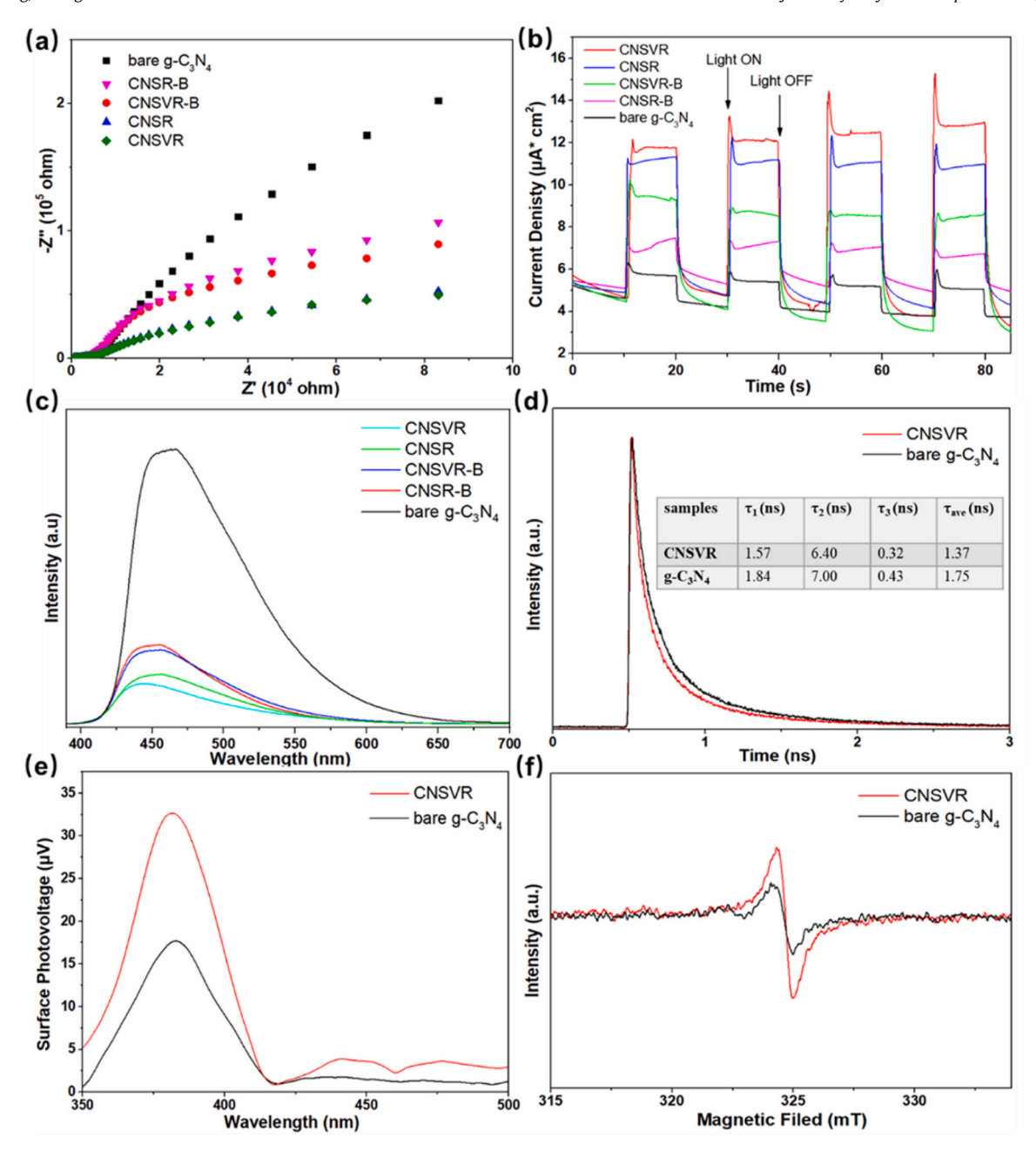


**Fig. 9.** (a) Nyquist plots, and (b) Photocurrent response curve of g- $C_3N_4$  and various kinds of g- $C_3N_4$ /ReSe $_2$  heterojunction samples, (c) steady-state (the inset in exhibits the charge carrier lifetimes) photoluminescence spectra, (d) transient-state photoluminescence spectra, (e) steady-state SPV spectra, and (f) EPR spectra in the visible light irradiation ( $\lambda > 420 \text{ nm}$ ) of bare g- $C_3N_4$  and CNSVR.

sample CNSVR showed increased EPR signals, which is compatible with the front results.

According to the foregoing discussions along with the kinetics studies [71–73] and investigations of some similar type heterojunction materials [64–67], the carrier transfer path and  $H_2$  evolution mechanism of the  $g\text{-}C_3N_4/\text{ReSe}_2(\text{SV})$  heterojunction in the photocatalytic process is proposed and explored, as shown in Fig. 10. The type-I heterojunction is formed first when the ReSe2 nanosheets are dispersed on  $g\text{-}C_3N_4$  due to their matching band structure. After visible-light irradiation, a substantial number of photoinduced electron–hole pairs will be formed inside the  $g\text{-}C_3N_4$  semiconductor. Simultaneously, since heterojunction forms between ReSe2(SV) nanosheets and  $g\text{-}C_3N_4$ , the CB potential absolute value of  $g\text{-}C_3N_4$ 

( $-0.97\,V$  vs. NHE) is higher than that of ReSe<sub>2</sub>(SV) ultrathin nanosheets ( $-0.36\,V$  vs. NHE), photoinduced electrons from the CB of g-C<sub>3</sub>N<sub>4</sub> quickly migrate to the CB of ReSe<sub>2</sub>(SV) ultrathin nanosheets and preferentially reduced to generate H<sub>2</sub> [74-77]. Because of the large mass gap between electron and hole [68], the vast majority of photogenerated holes remains on the g-C<sub>3</sub>N<sub>4</sub> surface and the holes will be removed by the sacrificial agent TEOA. This process is the key to separating holes and photogenerated electrons, suppressing the electron–hole pairs internal compounding. In addition, the Re-Se<sub>2</sub>(SV) ultrathin nanosheets and g-C<sub>3</sub>N<sub>4</sub> nanosheets formed a 2D spatial electron transport network, which greatly promoted the photo-induced electron transfer and separation, and obtained higher photocatalytic activity [34,35,78-80].

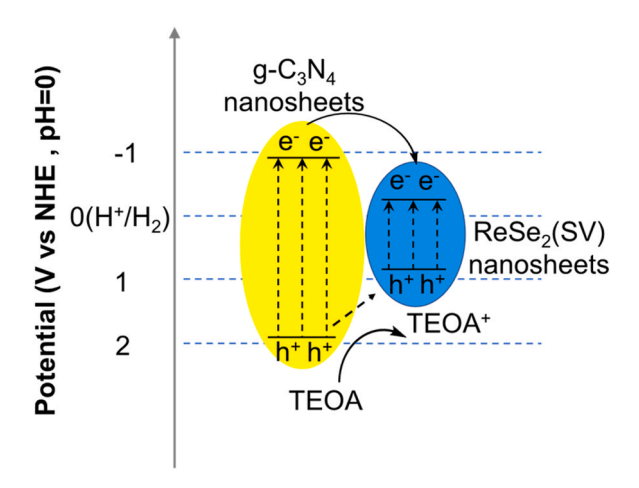


**Fig. 10.** Schematic energy-level diagrams and charge transfer mechanisms of CNSVR samples.

#### 4. Conclusion

In this work, the composite photocatalysts based on g-C<sub>3</sub>N<sub>4</sub> and ReSe<sub>2</sub> ultrathin nanosheets with abundant edge-active sites were synthesized via a simple and efficient ultrasound-assisted liquid stripping and self-assembly method. The experimental and theoretical investigations confirmed that there are intensive electronic interactions over the as-formed heterojunction between g-C<sub>3</sub>N<sub>4</sub> and ReSe<sub>2</sub>. Meanwhile, the ultrasonic treatment along with heterostructures led to the increase of edge active sites and significantly improved photocatalytic hydrogen production from water splitting. Simultaneously, the selenium vacancies in the photocatalyst improved the hydrogen production. Furthermore, the photocatalysis mechanism was explored in this work. Through optimization of the g-C<sub>3</sub>N<sub>4</sub>/ReSe<sub>2</sub> nanosheets, the hydrogen production rate increased 21 times from 50.18 to 1055.50  $\mu$ mol g<sup>-1</sup> h<sup>-1</sup> for pristine g-C<sub>3</sub>N<sub>4</sub> material and showed excellent stability in cycling and recovery experiments. The present study demonstrates that the electronic structure can be adjusted to increase the active sites by jointly reducing the number of nanosheet layers as well as by introducing vacancies. This method can be extended to various heterojunction photocatalysts of layered materials, since it is a promising method for designing solar photocatalysts for hydrogen production.

#### **CRediT** authorship contribution statement

**Zhengyun Wang:** Writing – original draft, Conceptualization, Visualization, Investigation. **Fengyi Yang:** Software, Validation, Data curation. **Ming-Hsien Lee:** Software, Validation, Data curation. **Tao Ding:** Writing – review & editing. **Qing Yang:** Funding acquisition, Project administration, Supervision, Writing – review & editing.

#### **Declaration of Competing Interest**

The authors declare that they have no known competing financial interests or personal relationships that could have appeared to influence the work reported in this paper.

#### Acknowledgements

This work was financially supported by the National Natural Science Foundation of China (U1932150 and 21571166). The numerical calculations in this paper have been done on the supercomputing system in the Supercomputing Center of University of Science and Technology of China. This research was also supported

by the advanced computing resources provided by the Supercomputing Center of the USTC.

#### Appendix A. Supporting information

Supplementary data associated with this article can be found in the online version at doi:10.1016/j.jallcom.2022.165786.

#### References

- [1] H. Nishiyama, T. Yamada, M. Nakabayashi, Y. Maehara, M. Yamaguchi, Y. Kuromiya, Y. Nagatsuma, H. Tokudome, S. Akiyama, T. Watanabe, R. Narushima, S. Okunaka, N. Shibata, T. Takata, T. Hisatomi, K. Domen, Photocatalytic solar hydrogen production from water on a 100 m<sup>2</sup> scale, Nature 598 (2021) 304–307.
- [2] M.Z. Rahman, M.G. Kibria, C.B. Mullins, Metal-free photocatalysts for hydrogen evolution, Chem. Soc. Rev. 49 (2020) 1887–1931.
- [3] W.J. Wang, C.Y. Zhou, Y. Yang, G.M. Zeng, C. Zhang, Y. Zhou, J.N. Yang, D.L. Huang, H. Wang, W.P. Xiong, X.P. Li, Y.K. Fu, Z.W. Wang, Q.Y. He, M.Y. Jia, H.Z. Luo, Carbon nitride based photocatalysts for solar photocatalytic disinfection, can we go further? Chem. Eng. J. 404 (2021) 126540.
- D. Clark, H. Malerod-Fjeld, M. Budd, I. Yuste-Tirados, D. Beeaff, S. Aamodt, K. Nguyen, L. Ansaloni, T. Peters, P.K. Vestre, D.K. Pappas, M.I. Valls, S. Remiro-Buenamanana, T. Norby, T.S. Bjorheim, J.M. Serra, C. Kjolseth, Single-step hydrogen production from NH<sub>3</sub>, CH<sub>4</sub>, and biogas in stacked proton ceramic reactors, Science 376 (2022) 390–393.
   C.X. Zhang, H.S. Nan, H.W. Tian, W.T. Zheng, Recent advances in pentlandites for
- [5] C.X. Zhang, H.S. Nan, H.W. Tian, W.T. Zheng, Recent advances in pentlandites for electrochemical water splitting: a short review, J. Alloy. Compd. 838 (2020) 155685.
- [6] T. Takata, J.Z. Jiang, Y. Sakata, M. Nakabayashi, N. Shibata, V. Nandal, K. Seki, T. Hisatomi, K. Domen, Photocatalytic water splitting with a quantum efficiency of almost unity, Nature 581 (2020) 411–414.
- [7] X.L. Song, G.F. Wei, J. Sun, C.D. Peng, J.L. Yin, X. Zhang, Y.L. Jiang, H.H. Fei, Overall photocatalytic water splitting by an organolead iodide crystalline material, Nat. Catal. 3 (2020) 1027–1033.
- [8] X. Zhang, H. Yi, Q. An, S.X. Song, Recent advances in engineering cobalt carbonate hydroxide for enhanced alkaline water splitting, J. Alloy. Compd. 887 (2021) 161405.
- [9] P. Zhou, H. Chen, Y. Chao, Q. Zhang, W. Zhang, F. Lv, L. Gu, Q. Zhao, N. Wang, J. Wang, S. Guo, Single-atom Pt-I<sub>3</sub> sites on all-inorganic Cs<sub>2</sub>SnI<sub>6</sub> perovskite for efficient photocatalytic hydrogen production, Nat. Commun. 12 (2021) 4412.
- [10] X. Han, L. An, Y. Hu, Y.G. Li, C.Y. Hou, H.Z. Wang, Q.H. Zhang, Ti<sub>3</sub>C<sub>2</sub> MXene-derived carbon-doped TiO<sub>2</sub> coupled with g-C<sub>3</sub>N<sub>4</sub> as the visible-light photocatalysts for photocatalytic H<sub>2</sub> generation, Appl. Catal. B-Environ. 265 (2020) 118539.
- [11] Y.C. Guo, L. Mao, Y. Tang, Q.Q. Shang, X.Y. Cai, J.Y. Zhang, H.L. Hu, X. Tan, L.Q. Liu, H.Y. Wang, T. Yu, J.H. Ye, Concentrating electron and activating H-OH bond of absorbed water on metallic NiCo<sub>2</sub>S<sub>4</sub> boosting photocatalytic hydrogen evolution, Nano Energy 95 (2022) 107028.
- [12] S. Goktas, A. Goktas, A comparative study on recent progress in efficient ZnO based nanocomposite and heterojunction photocatalysts: a review, J. Alloy. Compd. 863 (2021) 158734.
- [13] Y. Zhou, F. Lu, T.S. Fang, D.H. Gu, X.B. Feng, T.H. Song, W.C. Liu, A brief review on metal halide perovskite photocatalysts: History, applications and prospects, J. Alloy. Compd. 911 (2022) 165062.
- [14] X. Wang, K. Maeda, A. Thomas, K. Takanabe, G. Xin, J.M. Carlsson, K. Domen, M. Antonietti, A metal-free polymeric photocatalyst for hydrogen production from water under visible light, Nat. Mater. 8 (2009) 76–80.
- [15] F. He, Z.X. Wang, Y.X. Li, S.Q. Peng, B. Liu, The nonmetal modulation of composition and morphology of g-C<sub>3</sub>N<sub>4</sub> based photocatalysts, Appl. Catal. B-Environ. 269 (2020) 118828.
- [16] M. Ismael, A review on graphitic carbon nitride (g-C<sub>3</sub>N<sub>4</sub>) based nanocomposites: Synthesis, categories, and their application in photocatalysis, J. Alloy. Compd. 846 (2020) 156446.
- [17] Q.L. Xu, L.Y. Zhang, B. Cheng, J.J. Fan, J.G. Yu, S-scheme heterojunction photocatalyst, Chem. -Us 6 (2020) 1543-1559.
- [18] D.M. Zhao, Y.Q. Wang, C.L. Dong, Y.C. Huang, J. Chen, F. Xue, S.H. Shen, L.J. Guo, Boron-doped nitrogen-deficient carbon nitride-based Z-scheme heterostructures for photocatalytic overall water splitting, Nat. Energy 6 (2021) 388–397.
- [19] P. Babu, S.R. Dash, K. Parid, Mechanistic insight the visible light driven hydrogen generation by plasmonic Au-Cu alloy mounted on TiO<sub>2</sub> @B-doped g-C<sub>3</sub>N<sub>4</sub> heterojunction photocatalyst, J. Alloy Compd. 909 (2022) 164754.
- [20] A. Splendiani, L. Sun, Y. Zhang, T. Li, J. Kim, C.Y. Chim, G. Galli, F. Wang, Emerging Photoluminescence in Monolayer MoS<sub>2</sub>, Nano Lett. 10 (2010) 1271–1275.
- [21] J.R. Ran, H.P. Zhang, J.T. Qu, J.Q. Shan, S.M. Chen, F. Yang, R.K. Zheng, J. Cairney, L. Song, L.Q. Jing, S.Z. Qiao, Atomic-level insights into the edge active ReS<sub>2</sub> ultrathin nanosheets for high-efficiency light-to-hydrogen conversion, ACS Mater. Lett. 2 (2020) 1484–1494.
- [22] W.B. Li, L. Wang, Q. Zhang, Z.Y. Chen, X.Y. Deng, C. Feng, L.K. Xu, M.X. Sun, Fabrication of an ultrathin 2D/2D C<sub>3</sub>N<sub>4</sub>/MoS<sub>2</sub> heterojunction photocatalyst with enhanced photocatalytic performance, J. Alloy. Compd. 808 (2019) 151681.
- [23] N. Singh, G. Jabbour, U. Schwingenschlogl, Optical and photocatalytic properties of two-dimensional MoS<sub>2</sub>, Eur. Phys. J. B 85 (2012) 392.

- [24] M.H. Jiang, Y.J. Zou, F. Xu, L. Sun, J. Zhang, S. Yu, J. Zhang, C.L. Xiang, Synthesis of g-C<sub>3</sub>N<sub>4</sub>/Fe<sub>3</sub>O<sub>4</sub>/MoS<sub>2</sub> composites for efficient hydrogen evolution reaction, J. Alloy. Compd. 906 (2022) 164265.
- [25] E. Lorchat, G. Froehlicher, S. Berciaud, Splitting of interlayer shear modes and photon energy dependent anisotropic raman response in N-Layer ReSe<sub>2</sub> and ReS<sub>2</sub>, ACS Nano 10 (2016) 2752–2760.
- [26] A. Arora, J. Noky, M. Druppel, B. Jariwala, T. Deilmann, R. Schneider, R. Schmidt, O.D. Pozo-Zamudio, T. Stiehm, A. Bhattacharya, P. Kruger, S.M. de Vasconcellos, M. Rohlfing, R. Bratschitsch, Highly anisotropic in-plane excitons in atomically thin and bulklike 1T'-ReSe<sub>2</sub>, Nano Lett. 17 (2017) 3202–3207.
- [27] B. Jariwala, D. Voiry, A. Jindal, B.A. Chalke, R. Bapat, A. Thamizhavel, M. Chhowalla, M. Deshmukh, A. Bhattacharya, Synthesis and characterization of ReS<sub>2</sub> and ReSe<sub>2</sub> layered chalcogenide single crystals, Chem. Mater. 28 (2016) 3352–3359.
- [28] Y. Sun, J. Meng, H.X. Ju, J.F. Zhu, Q.X. Li, Q. Yang, Electrochemical activity of 1T structured rhenium selenide nanosheets via electronic structural modulation from selenium-vacancy generation, J. Mater. Chem. A 6 (2018) 22526–22533.
- [29] S.J. Clark, M.D. Segall, C.J. Pickard, P.J. Hasnip, M.J. Probert, K. Refson, M.C. Payne, First principles methods using CASTEP, Z. Krist. 220 (2005) 567–570.
- [30] J.P. Perdew, K. Burke, M. Ernzerhof, Generalized gradient approximation made simple, Phys. Rev. Lett. 77 (1996) 3865–3868.
- [31] D.D. Koelling, B. N. Harmon. A technique for relativistic spin-polarised calculations, J. Phys. C: Solid State Phys. 10 (1977) 3107–3114.
- [32] J.K. Norskov, T. Bligaard, A. Logadottir, J.R. Kitchin, J.G. Chen, S. Pandelov, J.K. Norskov, Trends in the exchange current for hydrogen evolution, J. Electrochem. Soc. 152 (2005) J23–J26.
- [33] F.L. Lai, W. Zong, G.J. He, Y. Xu, H.W. Huang, B. Weng, D.W. Rao, J.A. Martens, J. Hofkens, I.P. Parkin, T.X. Liu, N<sub>2</sub> electroreduction to NH<sub>3</sub> by selenium vacancy-rich ReSe<sub>2</sub> catalysis at an abrupt interface, Angew. Chem. Int. Ed. 59 (2020) 13320–13327
- [34] X. Chen, R. Shi, Q. Chen, Z. Zhang, W. Jiang, Y. Zhu, T. Zhang, Three-dimensional porous g-C<sub>3</sub>N<sub>4</sub> for highly efficient photocatalytic overall water splitting, Nano Energy 59 (2019) 644–650.
- [35] C. Xing, H. Zhao, G. Yu, L. Guo, Y. Hu, T. Chen, L. Jiang, X. Li, Modification of g-C<sub>3</sub>N<sub>4</sub> photocatalyst with flower-like ReS<sub>2</sub> for highly efficient photocatalytic hydrogen evolution, ChemCatChem 12 (2020) 6385–6392.
- [36] J.X. Li, Y.H. Wang, X.C. Li, Q.Q. Gao, S.D. Zhang, A facile synthesis of high-crystalline g-C<sub>3</sub>N<sub>4</sub> nanosheets with closed self-assembly strategy for enhanced photocatalytic H<sub>2</sub> evolution, J. Alloy. Compd. 881 (2021) 160551.
- [37] N. Nie, L. Zhang, J. Fu, B. Cheng, J. Yu, Self-assembled hierarchical direct Z-scheme g-C<sub>3</sub>N<sub>4</sub>/ZnO microspheres with enhanced photocatalytic CO<sub>2</sub> reduction performance, Appl. Surf. Sci. 441 (2018) 12–22.
   [38] J.W. Fu, Q.L. Xu, J.X. Low, C.J. Jiang, J.G. Yu, Ultrathin 2D/2D WO<sub>3</sub>/g-C<sub>3</sub>N<sub>4</sub> step-
- [38] J.W. Fu, Q.L. Xu, J.X. Low, C.J. Jiang, J.G. Yu, Ultrathin 2D/2D WO<sub>3</sub>/g-C<sub>3</sub>N<sub>4</sub> step-scheme H<sub>2</sub> production photocatalyst, Appl. Catal. B-Environ. 243 (2019) 556–565.
- [39] Y.W. Yuan, L.L. Zhang, J. Xing, M.I.B. Utama, X. Lu, K.Z. Du, Y.M. Li, X. Hu, S.J. Wang, A. Genc, R. Dunin-Borkowski, J. Arbiol, Q.H. Xiong, High-yield synthesis and optical properties of  $g-C_3N_4$ , Nanoscale 7 (2015) 12343–12350.
- [40] X.Y. Yu, N. Guijarro, M. Johnson, K. Sivula, Defect mitigation of solution-processed 2D WSe<sub>2</sub> nanoflakes for solar-to-hydrogen conversion, Nano Lett. 18 (2018) 215–222.
- [41] Y. Sun, X.W. Zhang, B.G. Mao, M.H. Cao, Controllable selenium vacancy engineering in basal planes of mechanically exfoliated WSe<sub>2</sub> monolayer nanosheets for efficient electrocatalytic hydrogen evolution, Chem. Commun. 52 (2016) 14266–14269.
- [42] A. Cimino, B.A. Deangelis, D. Gazzoli, M. Valigi, Photoelectron-spectroscopy (XPS) and thermogravimetry (Tg) of pure and supported rhenium oxides pure rhenium compounds, Z. Anorg. Allg. Chem. 460 (1980) 86–98.
- [43] S. Kim, H.K. Yu, S. Yoon, N.S. Lee, M.H. Kim, Growth of two-dimensional rhenium disulfide (ReS<sub>2</sub>) nanosheets with a few layers at low temperature, Crystengcomm 19 (2017) 5341–5345.
- [44] S. Yang, S. Tongay, Y. Li, Q. Yue, J. Xia, S. Li, J. Li, S. Wei, Layer-dependent electrical and optoelectronic responses of ReSe<sub>2</sub> nanosheet transistors, Nanoscale 6 (2014) 7226.
- [45] X.B. Li, B.B. Kang, F. Dong, Z.Q. Zhang, X.D. Luo, L. Han, J.T. Huang, Z.J. Feng, Z. Chen, J.L. Xu, B.L. Peng, Z.L. Wang, Enhanced photocatalytic degradation and H<sub>2</sub>/H<sub>2</sub>O<sub>2</sub> production performance of S-pCN/WO<sub>2.72</sub> S-scheme heterojunction with appropriate surface oxygen vacancies, Nano Energy 81 (2021) 105671.
- [46] K.T. Feng, J.Z. Tian, X.Y. Hu, J. Fan, E.Z. Liu, Active-center-enriched Ni<sub>0.85</sub>Se/g-C<sub>3</sub>N<sub>4</sub> S-scheme heterojunction for efficient photocatalytic H<sub>2</sub> generation, Int. J. Hydrogen Energy 47 (2022) 4601–4613.
- [47] M.J. Wang, S.L. Shen, L. Li, Z.H. Tang, J.H. Yang, Effects of sacrificial reagents on photocatalytic hydrogen evolution over different photocatalysts, J. Mater. Sci. 52 (2017) 5155–5164.
- [48] L. Chen, Y.M. Xu, Z. Yang, K. Zhang, B.L. Chen, Cobalt (II)-based open-framework systems constructed on g-C<sub>3</sub>N<sub>4</sub> for extraordinary enhancing photocatalytic hydrogen evolution, Appl. Catal. B-Environ. 277 (2020) 119207.
- [49] V. Kumaravel, M.D. Imam, A. Badreldin, R.K. Chava, J.Y. Do, M. Kang, A. Abdel-Wahab, Photocatalytic hydrogen production: role of sacrificial reagents on the activity of oxide, carbon, and sulfide catalysts, Catalysts 9 (2019) 9030276.
- [50] X.B. Chen, S.H. Shen, L.J. Guo, S.S. Mao, Semiconductor-based photocatalytic hydrogen generation, Chem. Rev. 110 (2010) 6503–6570.
- [51] H.S. Moon, K.J. Yong, Noble-metal free photocatalytic hydrogen generation of CuPc/TiO<sub>2</sub> nanoparticles under visible-light irradiation, Appl. Surf. Sci. 530 (2020) 147215.

- [52] C.P. Bai, J.C. Bi, J.B. Wu, H. Meng, Y. Xu, Y.D. Han, X. Zhang, Fabrication of noble-metal-free g-C<sub>3</sub>N<sub>4</sub>-MIL-53(Fe) composite for enhanced photocatalytic H<sub>2</sub> generation performance, Appl. Organomet. Chem. 32 (2018) 4597.
- [53] D. Kim, K. Yong, Boron doping induced charge transfer switching of a C<sub>3</sub>N<sub>4</sub>/ZnO photocatalyst from Z-scheme to type II to enhance photocatalytic hydrogen production, Appl. Catal. B-Environ. 282 (2021) 119538.
- [54] X.Y. Ji, R.T. Guo, Z.D. Lin, L.F. Hong, Y. Yuan, W.G. Pan, A NiS co-catalyst decorated Zn<sub>3</sub>ln<sub>2</sub>S<sub>6</sub>/g-C<sub>3</sub>N<sub>4</sub> type-II ball-flower-like nanosphere heterojunction for efficient photocatalytic hydrogen production, Dalton Trans. 50 (2021) 11249–11258.
- [55] Z.F. Huang, J.J. Song, X. Wang, L. Pan, K. Li, X.W. Zhang, L. Wang, J.J. Zou, Switching charge transfer of C<sub>3</sub>N<sub>4</sub>/W<sub>18</sub>O<sub>49</sub> from type-II to Z-scheme by interfacial band bending for highly efficient photocatalytic hydrogen evolution, Nano Energy 40 (2017) 308–316.
- [56] J.H. Zhang, J.C. Liu, W. Zhao, Z.X. Ding, J.J. Mai, Y.X. Fang, Facile synthesis of high quality Z-scheme W<sub>18</sub>O<sub>49</sub> nanowire-g-C<sub>3</sub>N<sub>4</sub> photocatalyst for the enhanced visible light-driven photocatalytic hydrogen evolution, J. Alloy. Compd. 764 (2018) 1–9.
- [57] Y. Guo, B. Chang, T. Wen, S. Zhang, M. Zeng, N. Hu, Y. Su, Z. Yang, B. Yang, A Z-scheme photocatalyst for enhanced photocatalytic H<sub>2</sub> evolution, constructed by growth of 2D plasmonic MoO<sub>3-x</sub> nanoplates onto 2D g-C<sub>3</sub>N<sub>4</sub> nanosheets, J. Colloid Interface Sci. 567 (2020) 213–223.
- [58] Z.L. Huang, J.C. Liu, S. Zong, X.Y. Wang, K.X. Chen, L.L. Liu, Y.X. Fang, Fabrication of graphitic carbon Nitride/Nonstoichiometric molybdenum oxide nanorod composite with the nonmetal plasma enhanced photocatalytic hydrogen evolution activity, J. Colloid Interface Sci. 606 (2022) 848–859.
- [59] Y.F. Pan, B. Xiong, Z. Li, Y. Wu, C.J. Yan, H.B. Song, In situ constructed oxygen–vacancy-rich MoO<sub>3-x/</sub>porous g-C<sub>3</sub>N<sub>4</sub> heterojunction for synergistically enhanced photocatalytic H<sub>2</sub> evolution, Rsc Adv. 11 (2021) 31219–31225.
- [60] G.M. Dong, Y.W. Zhang, Y.Y. Wang, Q.H. Deng, C.C. Qin, Y.J. Hu, Y.M. Zhou, G.K. Tian, Ti<sub>3</sub>C<sub>2</sub> quantum dots modified 3D/2D TiO<sub>2</sub>/g-C<sub>3</sub>N<sub>4</sub> S-scheme heterostructures for highly efficient photocatalytic hydrogen evolution, ACS Appl. Energ. Mater. 4 (2021) 14342–14351.
- [61] W. Qian, S. Xu, X. Zhang, C. Li, W. Yang, C.R. Bowen, Y. Yang, Differences and similarities of photocatalysis and electrocatalysis in two-dimensional nanomaterials: strategies, traps, applications and challenges, Nanomicro Lett. 13 (2021) 156.
- [62] X.L. Zhou, Y. Liu, H.X. Ju, B.C. Pan, J.F. Zhu, T. Ding, C.D. Wang, Q. Yang, Design and epitaxial growth of MoSe<sub>2</sub>-NiSe vertical heteronanostructures with electronic modulation for enhanced hydrogen evolution reaction, Chem. Mater. 28 (2016) 1838–1846.
- [63] J. Yang, C.D. Wang, H.X. Ju, Y. Sun, S.Q. Xing, J.F. Zhu, Q. Yang, Integrated quasiplane heteronanostructures of MoSe<sub>2</sub>/Bi<sub>2</sub>Se<sub>3</sub> hexagonal nanosheets: synergetic electrocatalytic water splitting and enhanced supercapacitor performance, Adv. Funct. Mater. 27 (2017) 1703864.
- [64] C.B. Liu, L.L. Wang, Y.H. Tang, S.L. Luo, Y.T. Liu, S.Q. Zhang, Y.X. Zeng, Y.Z. Xu, Vertical single or few-layer MoS<sub>2</sub> nanosheets rooting into TiO<sub>2</sub> nanofibers for highly efficient photocatalytic hydrogen evolution, Appl. Catal. B-Environ. 164 (2015) 1–9.
- [65] X.H. Ma, C.J. Ren, H.D. Li, X.T. Liu, X.Y. Li, K. Han, W.J. Li, Y.F. Zhan, A. Khan, Z.D. Chang, C.Y. Sun, H.L. Zhou, A novel noble-metal-free Mo<sub>2</sub>C-In<sub>2</sub>S<sub>3</sub> heterojunction photocatalyst with efficient charge separation for enhanced photocatalytic H<sub>2</sub> evolution under visible light, J. Colloid Interface Sci. 582 (2021) 488–495.
- [66] J.J. Yi, H.P. Li, Y.J. Gong, X.J. She, Y.H. Song, Y.G. Xu, J.J. Deng, S.Q. Yuan, H. Xu, H.M. Li, Phase and interlayer effect of transition metal dichalcogenide cocatalyst toward photocatalytic hydrogen evolution: the case of MoSe<sub>2</sub>, Appl. Catal. B-Environ. 243 (2019) 330–336.
- [67] Z.F. Huang, J.J. Song, L. Pan, Z.M. Wang, X.Q. Zhang, J.J. Zou, W.B. Mi, X.W. Zhang, L. Wang, Carbon nitride with simultaneous porous network and O-doping for efficient solar-energy-driven hydrogen evolution, Nano Energy 12 (2015) 646–656.
- [68] G.H. Dong, Z.H. Ai, L.Z. Zhang, Efficient anoxic pollutant removal with oxygen functionalized graphitic carbon nitride under visible light, RSC Adv. 4 (2014) 5553–5560.
- [69] K. Sun, M. Liu, J. Pei, D. Li, C. Ding, K. Wu, H. Jiang, Incorporating transition–metal phosphides into metal-organic frameworks for enhanced photocatalysis, Angew. Chem. Int. Ed. 59 (2020) 2–9.
- [70] J.H. Sun, J.S. Zhang, M.W. Zhang, M. Antonietti, X.Z. Fu, X.C. Wang, Bioinspired hollow semiconductor nanospheres as photosynthetic nanoparticles, Nat. Commun. 3 (2012) 1139.
- [71] R.T. Chen, S. Pang, H.Y. An, J. Zhu, S. Ye, Y.Y. Gao, F.T. Fan, C. Li, Charge separation via asymmetric illumination in photocatalytic Cu<sub>2</sub>O particles, Nat. Energy 3 (2018) 655–663.
- [72] Z.W. Chen, Q. Zhang, Y. Luo, Experimental identification of ultrafast reverse hole transfer at the interface of the photoexcited methanol/graphitic carbon nitride system, Angew. Chem. Int. Ed. 57 (2018) 5320–5324.
- [73] W.C. Wang, Y. Tao, L.L. Du, Z. Wei, Z.P. Yan, W.K. Chan, Z.C. Lian, R.X. Zhu, D.L. Phillips, G.S. Li, Femtosecond time-resolved spectroscopic observation of long-lived charge separation in bimetallic sulfide/g-C<sub>3</sub>N<sub>4</sub> for boosting photocatalytic H<sub>2</sub> evolution, Appl. Catal. B-Environ. 282 (2021) 119568.
- [74] X.H. Ma, W.J. Li, C.J. Ren, H.D. Li, X.Y. Li, M. Dong, Y. Gao, T.Y. Wang, H.L. Zhou, Y.Y. Li, Fabrication of novel noble-metal-free Znln<sub>2</sub>S<sub>4</sub>/WC Schottky junction heterojunction photocatalyst: efficient charge separation, increased active sites and low hydrogen production overpotential for boosting visible-light H<sub>2</sub> evolution, J. Alloy. Compd. 901 (2022) 163709.

- [75] X. Ma, W. Li, H. Li, M. Dong, X. Li, L. Geng, H. Fan, Y. Li, H. Qiu, T. Wang, Fabrication of novel and noble-metal-free MoP/ $\ln_2 S_3$  Schottky heterojunction
- Fabrication of novel and noble-metal-free MoP/In<sub>2</sub>S<sub>3</sub> Schottky heterojunction photocatalyst with efficient charge separation for enhanced photocatalytic H<sub>2</sub> evolution under visible light, J. Colloid Interface Sci. 617 (2022) 284–292.

  [76] X.H. Ma, W.J. Li, C.J. Ren, H.D. Li, X.T. Liu, X.Y. Li, T.Y. Wang, M. Dong, S.J. Liu, S.W. Chen, A novel noble-metal-free binary and ternary In<sub>2</sub>S<sub>3</sub> photocatalyst with WC and "W-Mo auxiliary pairs" for highly-efficient visible-light hydrogen evolution, J. Alloy. Compd. 875 (2021) 160058.
- [77] M. Muska, J. Yang, Y. Sun, J.H. Wang, Y. Wang, Q. Yang, CoSe<sub>2</sub> nanoparticles dispersed in WSe<sub>2</sub> nanosheets for efficient electrocatalysis and supercapacitance applications, ACS Appl. Nano Mater. 4 (2021) 5796–5807.
- [78] Q. Zhu, Z. Xu, B. Qiu, M. Xing, J. Zhang, Emerging cocatalysts on g-C<sub>3</sub>N<sub>4</sub> for photocatalytic hydrogen evolution, Small 17 (2021) 2101070.
  [79] M. Li, S. Yu, H. Huang, X. Li, Y. Feng, C. Wang, Y. Wang, T. Ma, L. Guo, Y. Zhang, Unprecedented eighteen-faceted BiOCl with a ternary facet junction boosting cascade charge flow and photo-redox, Angew. Chem. Int Ed. 58 (2019) 9517-9521.
- [80] M.X. Tan, C.Y. Yu, J.J. Li, Y. Li, C.D. Tao, C.B. Liu, H.M. Meng, Y.J. Su, L.J. Qiao, Y. Bai, Engineering of g-C<sub>3</sub>N<sub>4</sub>-based photocatalysts to enhance hydrogen evolution, Adv. Colloid Interface 295 (2021) 102488.